A Comparative Study of Power Supply Architectures in Wireless EV Charging Systems

Bryan Esteban, *Member, IEEE*, Maher Sid-Ahmed, and Narayan C. Kar, *Senior Member, IEEE*

***Abstract*—This paper examines two of the primary power supply architectures being predominantly used for wireless electric vehicle (EV) charging, namely the series LC (SLC) resonant and the hybrid series–parallel (*LCL*) resonant full-bridge inverter topologies. The study of both of these topologies is presented in the context of designing a 3-kW primary-side controlled stationary wireless EV charger with nominal operating parameters of 30-kHz center frequency, a range of coupling in the neighborhood of 0.18–0.26, and a parallel secondary pick-up with partial series coil compensation. A comparison of both architectures is made in terms of their design methodology, physical size, cost, complexity, and efficiency. It is found that the SLC architecture is 2.45% less costly than the *LCL* topology. On the other hand, it is observed that the *LCL* architecture achieves almost 10% higher peak efficiency at rated load and minimum coupling. The study also showed that the SLC topology suffers from poor light load efficiency, while the *LCL* topology maintains very high efficiency over its full range of coupling and loading. The study also revealed that the capacitor voltage stress is significantly higher in the SLC topology. Finally, it is also shown that the control complexity of the SLC architecture is higher than that of the *LCL* architecture because of its sensitivity to changes in the reflected secondary impedance, which result in loss of constant current source and ZVS operation unless a suitable combination of parameters are modulated by the closed-loop controller.**

***Index Terms*—Inductive power transfer (IPT), LCL power supply, resonant inverter, SLC power supply, wireless EV charging.**

NOMENCLATURE

R_L	Load resistance.
$R_{\rm eq}$	Equivalent load resistance through rectifier in a continuous-conduction mode.
P	Power.
$P_{\max}$	Maximum power.
L_1	Primary pad inductance.
L_2	Secondary pad inductance.
M	Coupled-pad mutual inductance.
k	Magnetic coupling coefficient.
C_2	Secondary resonant tuning capacitor.
C_{S2}	Secondary coil partial series tuning capacitor.
C_{S1}	Primary coil partial series tuning capacitor for *LCL* topology.
C_1	Primary resonant tuning capacitor.
C_B	HF transformer dc-blocking capacitor.
$L_{2\rm eq}$	Equivalent secondary inductance when partial series compensation is used.
$L_{2\rm eq}$	Equivalent primary inductance when partial series compensation is used.
ω	Operating angular frequency.
ω_0	Resonant angular frequency.
V_U	Utility input voltage.
V_S	Fundamental of inverter voltage.
Z_r	Reflected secondary impedance.
$R_r\ (M, R_{\rm eq})$	Reflected secondary resistance.
$C_r\ (M)$	Reflected secondary capacitance.
Q_{2t}	Overall tunned secondary quality factor.
Q_{2v}	Secondary voltage boost quality factor.
Q_{2i}	Secondary current boost quality factor.
Q_u	Unloaded magnetic pad quality factor.
I_1	Primary current.
I_B	Inverter bridge current.
I_{C2}	*LCL* parallel capacitor current.
I_2	Secondary current.
I_{C2}	Secondary parallel capacitor current.
$I_{\rm sc}$	Secondary short-circuit current.
I_L	Load current.
$V_{\rm LB}$	*LCL* bridge inductor voltage.
V_{C1}	*LCL* parallel capacitor voltage or SLC series capacitor voltage.
V_{CS1}	*LCL* partial series tuning capacitor voltage.
V_{L1}	Primary coil voltage.
V_{L2}	Secondary coil voltage.
V_{CS2}	Partial series tuning capacitor voltage.
V_{C2}	Secondary parallel capacitor voltage. $V_{L2\rm oc}$
$V_{L2\rm oc}$	Secondary coil open-circuit voltage.
X_{L1}	Effective reactance of primary coil with partial series compensation.
$t_{\rm PS}$	Phase-shift time delay between inverter legs A and B.
t_d	Dead time between series bridge semiconductors.
$t_{\rm on}$	Time duration of semiconductor conduction interval.
$t_{\rm off}$	Time duration of semiconductor non-conduction interval.
T_s	Switching time period.
N_1	Isolation transformer number of primary turns.
N_2	Isolation transformer number of secondary turns.

Manuscript received September 29, 2014; revised December 21, 2014 and May 3, 2015; accepted May 18, 2015. Date of publication June 8, 2015; date of current version July 10, 2015. Recommended for publication by Associate Editor Y. J. Jang.

The authors are with the Department of Electrical and Computer Engineering, University of Windsor, Windsor, ON N9B 3P4, Canada (e-mail: bryan.esteban@gmail.com; ahmed@uwindsor.ca; nkar@uwinsor.ca).

Color versions of one or more of the figures in this paper are available online at http://ieeexplore.ieee.org.

Digital Object Identifier 10.1109/TPEL.2015.2440256

I. Introduction

WIRELESS inductive power transfer (IPT)—also known more generally as wireless power transfer—is an emerging technology that uses time-varying magnetic fields to transfer power over large air gaps to energize or charge one or more electrical loads with high efficiency. This novel and disruptive technology has been quietly maturing in research labs over the past two decades and is now poised to redefine the way electrical power is consumed by society at large.

To date, IPT has been successfully adopted in clean rooms and industrial manufacturing floors for powering automated guided vehicles that are constrained to travel over a track and can require multikilowatt levels of power to operate [1]–[5]. It has also been used to transfer small amounts of power over small air gaps for charging of portable consumer electronics, such as cell phones, tablets, and electric tooth brushes [6]–[9].

More recently though, the application of this technology for static and in-motion charging of electrified transportation, such as electric vehicles, buses, and train systems over larger air gaps and misalignment has seen an explosion in research and development in academia and private industry [10]–[27]. The adoption of wireless EV charging is viewed by many as a viable mechanism for extending the range of EVs and reducing the high cost associated with their large battery packs [14], [28]–[30]. With an interoperability industry standard (SAEJ2954) well in progress toward completion by 2015, wireless charging of EVs has gone from being merely an obscure and exotic technology to a tangible and appealing reality [31]–[33].

The successful deployment and mass adoption of wireless EV charging depends greatly on achieving high end-to-end system efficiency (85–90%) so as to be on par with existing conductive charging technologies. This requirement means that all subsystems in the cascade must have efficiencies in the order of 96–97% [34]. A critical subsystem to the overall efficiency is the primary power supply [22].

A survey of the literature reveals that two primary-side power supply architectures are predominantly being used for wireless EV charging systems, namely the series LC (SLC) resonant and the hybrid series–parallel resonant (*LCL*) topologies [13], [14], [17]–[23], [35]–[44]. The published works on these two topologies offer excellent insights into the fundamental operation, desirable features, and limitations of each for the application at hand, but because of differences in the system operating frequency, secondary side topology, control scheme, range of coupling and loading, as well as the use of different discrete components in the physical implementation of common subsystems, a true performance comparison of the two architectures cannot be made. The importance and practical value of being able to compare the performance of the aforesaid architectures is discernible from the fact that one of the key objectives of the J2954 task force is the recommendation of a standard primary power supply topology [32]. In view of the foregoing, this paper has as its goal the completion of a comparative study of the SLC and *LCL* power supplies under identical operating conditions typical in stationary wireless EV charging applications.

The remainder of the paper is organized as follows. Section II presents an overview of the typical wireless EV charger and associated theoretical concepts. Section III outlines the design and characterization of the magnetic pads used for the physical implementation completed in this study. Section IV presents an overview of the fundamental operation, desirable features, limitations, and design strategy of each of the two architectures being compared. Section V reviews the overall strategy adopted in the design of the complete wireless charging system used in the comparison. Section VI presents the results of the comparative study, and, finally, Section VII recaps the key outcomes of the comparison.

II. Wireless EV Charger Overview

As shown in Fig. 1, a typical inductive EV charging system is made up of two electrically isolated entities known as the primary and the secondary sides. The primary side can be further partitioned into the following subsystems.

1) *Utility Input:* Low-frequency energy source, which could be single phase as in Fig. 1 or three phase.
2) *AC/DC:* Power conditioner that in addition to converting the utility input to a regulated dc voltage, carries out power factor correction, and serves as one of the control mechanisms for regulating the power flow of the entire system by modulating the dc input voltage [23], [34].
3) *DC/AC:* Voltage fed full-bridge switching network that efficiently converts the incoming dc energy to high-frequency (HF) energy. It produces a HF square wave with fundamental component equal to the chosen operating frequency. Usually the bridge semiconductors are switched in accord with the phase-shift (PS) scheme illustrated in Fig. 1, allowing for power flow regulation through modulation of the PS delay time t_{PS} between each leg of the inverter. The semiconductors used in the implementation of this paper are MOSFETs, accordingly, the parallel capacitors and diodes across each switch in Fig. 1 are the parasitic elements of each device [13], [17], [23], [36], [39], [40].
4) *Isolation:* HF transformer required for compliance with regulatory safety standards. This stage could be implemented with a step-up or step-down transformer depending on the energy-coupling network (ECN) topology being used. The capacitor C_B is a dc-blocking capacitor that prevents transformer saturation and depending on the power supply topology may also be used to adjust the effective inductance of the transformer to some desired amount which is then used as one of the energy storage elements in the next stage [34], [36], [37], [45].
5) *Matching:* A network of very low-loss (high Q) energy storage elements used to efficiently inject the HF energy to the next stage and by extension lower the volt–ampere (VA) rating of the power supply. This stage is also commonly referred to as an impedance matching network (IMN), a resonant tank, bandpass filter, or a compensation network depending on the feature being highlighted in [11], [21], [46], and [23].

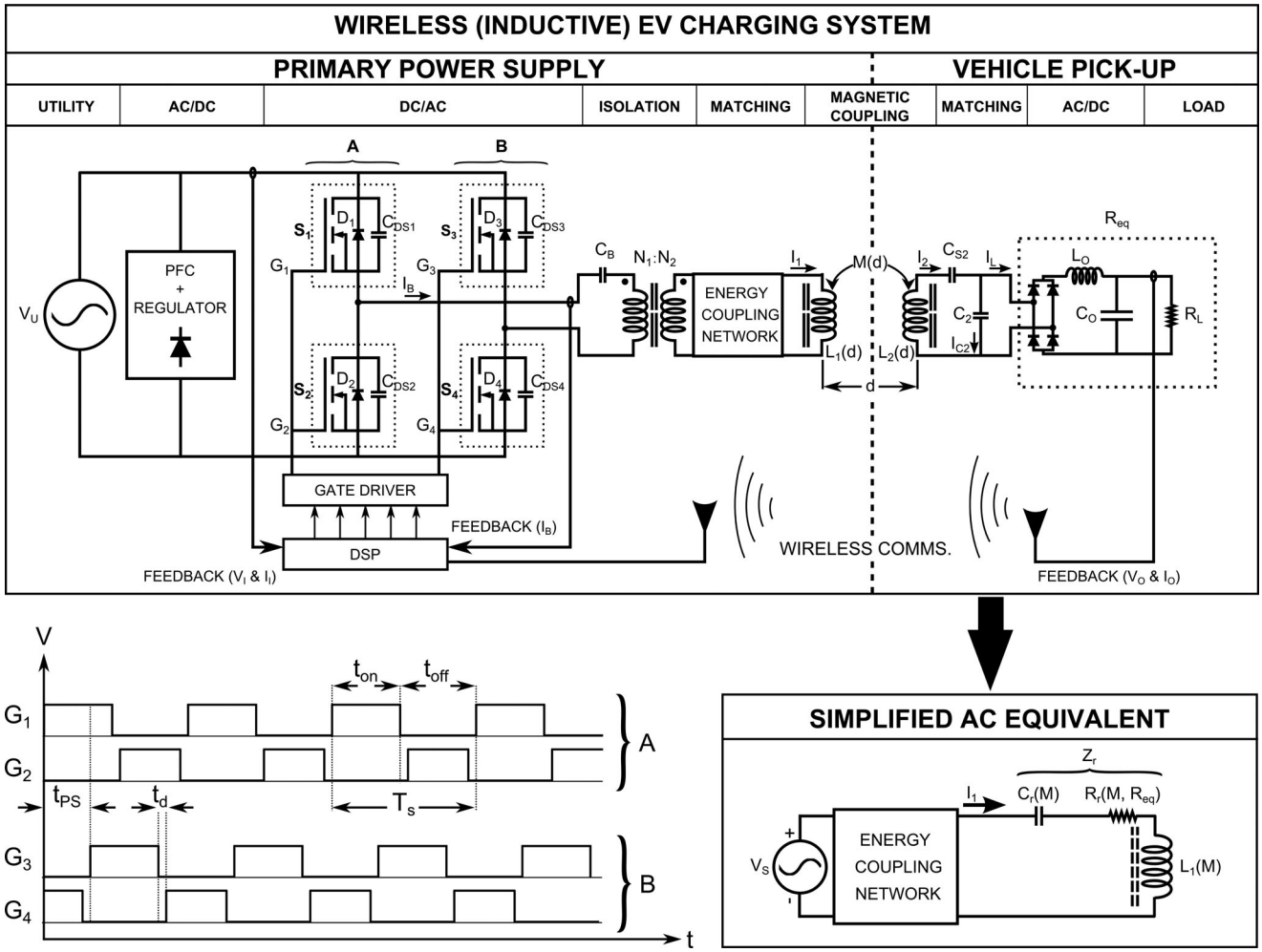

Fig. 1. Wireless EV charger, simplified equivalent referenced to the primary side, and PS gate driver pulse pattern.

In the literature, the first five blocks are commonly lumped together and referred to as the IPT power supply [47], [48].

Across a large and variable air gap, the secondary side can be similarly subdivided into an interconnection of the following subsystems.

1) *Matching:* Another network of energy storage elements that serves the same purpose as the one on the primary side. Though a number of different topologies are possible, [11], [12], [49], a parallel resonant arrangement with partial series compensation was chosen for this study because it is a commonly used topology for EV charging due of its constant current source characteristics [11], [20], [23], [49]. The addition of a capacitor in series with an inductor and deliberate operation above resonance so as to reduce or trim the overall inductive reactance to some smaller value is called partial series compensation. Partial series compensation is often used in IPT systems with parallel resonant topologies so as to trim the primary and/or secondary coil self-inductance to some lower value that is then resonated with a parallel capacitor [50], [51]. Capacitor C_{S2} in Fig. 1 is used for partial series compensation of the secondary coil. In a practical design, the use of partial series compensation on the secondary coil may serve one or both of the following purposes: 1) reducing the VA rating of the components connected to the resonant tank, and/or 2) boosting the current out of the secondary coil, thereby enhancing its power delivery capabilities. The later function is often carried out during the physical implementation's fine-tuning stage, where there is often a need to increase I_2 to achieve the design's target power level, but the pick-up coil's magnetic characteristics have already been largely fixed by its construction. It is relevant to note that for the parallel secondary topology, the maximum load current that may be delivered without the use of partial series compensation occurs when the pick-up is perfectly tuned and is equal to I_{sc}, where I_{sc} is the short-circuit current that would flow in the secondary coil if it were shorted, while coupled to the primary.
2) *AC/DC:* A HF rectifier with an output *LC* filter that provides the dc power to the vehicle battery. While other alternative ac/dc power conversion schemes can be implemented on the secondary side so as to actively shape the power flow, the simple HF rectifier with *LC* filter was chosen for this study because it results in a reduced cost

and complexity on vehicle side system integration [19], [20].

Common to both primary and secondary is the magnetic coupling stage. On the primary side, an inductive structure, commonly referred to as a magnetic pad or coupler, generates the ac magnetic flux that couples power to the secondary. Conversely, on the secondary side, another inductive structure, commonly referred to as a pick-up, captures a fraction of the primary flux. The size and geometry of the two coils may be identical or completely different. Like the primary- and secondary-side IMNs, this stage is also designed so as to have the highest possible unloaded quality factor, which generally means the use of a stranded Litz conductor, with the total number of strands and gauge of each strand sized so as to minimize the ac loss at the operating frequency [10], [42].

As highlighted in the magnetic coupling stage of Fig. 1, the mutual inductance and the primary and secondary coil self-inductances vary as a function of position, this fact plays an important role in the design of the power supply [1], [23], [52].

Fig. 1 also shows the wireless communication feedback mechanism used to close the control loop in order to actively regulate the power flow due to positional changes between the source and sink coils and/or changes in loading [21], [23].

With respect to Fig. 1 provided that the output inductor L_o is large enough to ensure continuous conduction of the rectifier diodes over the system's full range of operation, then the following relation holds true [23]

$$R_{\rm eq} = \frac{\pi^2 R_L}{8}. \tag{1}$$

As illustrated by the ac equivalent circuit in Fig. 1, at steady state, the entire system may be greatly simplified for analysis and design by replacing the primary-side power electronics with a sinusoidal voltage source v_S and reflecting the secondary side to the primary, which results in a reflected impedance Z_r in series with the primary coil.

The simplified input voltage may be expressed as

$$v_S = V_S \times \sin(2\pi f_0 t). \tag{2}$$

The RMS amplitude of v_S is related to the FB's dC-bus input voltage $V_{\rm DC}$, the operating frequency ω, and the PS control delay $t_{\rm PS}$, as follows:

$$V_S = \frac{2\sqrt{2}V_{\rm DC}}{\pi}\sin\left(\frac{\omega_0 \times t_{\rm PS}}{2}\right). \tag{3}$$

The reduction of the primary-side power electronics to a sinusoidal voltage source is commonly referred to as fundamental-mode analysis (FMA). The application of FMA to power electronic converters, and in particular to IPT systems, is a very well-established practice in the literature and is possible because the resonant networks that are connected to the output of the FB have significant filtering capability, which effectively reject all harmonics with the exception of the fundamental component of the HF square-wave inverter output [13], [23], [48], [53], [54].

The second simplification may be achieved by the application of standard circuit analysis techniques at the secondary followed by the application of the mutual inductance circuit model to reflect the secondary to the primary [11], [46], [55].

When a parallel secondary is reflected to the primary, it presents an impedance Z_r to the primary power supply. For a given frequency, the real and imaginary parts of Z_r are both functions of the variable mutual inductance M and the load $R_{\rm eq}$. The variability in M results from changes in alignment between the coils, while the variability of the load is due to changes in the battery's voltage and current profiles as it charges. Moreover, the imaginary part of Z_r is capacitive in nature [1], [56].

The reflected impedance seen at the primary can be shown as

$$Z_r = R_r\left(M, R_{\rm eq}\right) - j\frac{1}{\omega C_r\left(M, R\text{eq}\right)} \tag{4}$$

$$R_r\left(M, R_{\rm eq}\right) = \frac{R_{\rm eq}(\omega M)^2[\omega^2 C_2 L_{2\rm eq} - (\omega^2 C_2 L_{2\rm eq} - 1)]}{R_{\rm eq}^2(\omega^2 C_2 L_{2\rm eq} - 1)^2 + (\omega L_{2\rm eq})^2} \tag{5}$$

$$C_r\left(M, R_{\rm eq}\right) = \left[\frac{\omega^4 M^2[C_2 R_{\rm eq}^2(\omega^2 C_2 L_{2\rm eq} - 1) + L_{2\rm eq}]}{R_{\rm eq}^2(\omega^2 C_2 L_{2\rm eq} - 1)^2 + (\omega L_{2\rm eq})^2}\right]^{-1} \tag{6}$$

where $L_{2\rm eq}$ is the equivalent secondary coil's inductance after application of partial series compensation

$$L_{2\rm eq} = L_2 - \frac{1}{\omega^2 C_{S2}} = \frac{\omega^2 L_2 C_{S2} - 1}{\omega^2 C_{S2}}. \tag{7}$$

The power that is, thus, delivered by the RMS primary current to the reflected load is given by

$$\begin{aligned} P =& \ {\rm Re}\{I_1^2 Z_r\} \\ =& \ \frac{R_{\rm eq}(\omega M I_1)^2[\omega^2 C_2 L_{2\rm eq} - (\omega^2 C_2 L_{2\rm eq} - 1)]}{R_{\rm eq}^2(\omega^2 C_2 L_{2\rm eq} - 1)^2 + (\omega L_{2\rm eq})^2}. \end{aligned} \tag{8}$$

If the system is operated at or close to the secondary's resonant frequency

$$\omega_0 = \frac{1}{\sqrt{L_{2\rm eq} C_2}} \tag{9}$$

the term $\omega^2 L_{2\rm eq} C_2$ will be equal or very close to one. When this happens (4) and (8) become

$$Z_r = \frac{\omega_0 M^2 Q_{2v}}{L_{2\rm eq}} - j\frac{\omega_0 M^2}{L_{2\rm eq}} \tag{10}$$

$$P = \frac{\omega_0 (M I_1)^2 Q_{2v}}{L_{2\rm eq}} \tag{11}$$

where Q_{2v} is known as the voltage boost quality factor, and is defined as

$$Q_{2v} = \frac{R_{\rm eq}}{\omega L_{2\rm eq}}. \tag{12}$$

As can be discerned from (10), and as is depicted in the simplified ac equivalent circuit of Fig. 1, when the system is operated at resonance, the dependence of the reflected capactive reactance on the load is eliminated. Equation (11) is conventionally known as the IPT power equation, and it is deemed by

many authors as the starting point for the design of a resonant IPT system [1], [4], [23]. In theory, the minimum RMS primary current required to transfer a desired maximum amount of power $P_{\max}$, when the system is operated at resonance is equal to

$$I_1 = \sqrt{\frac{P_{\max} L_{2\mathrm{eq}}}{\omega_0 M^2 Q_{2v}}}. \tag{13}$$

The application of partial series compensation to the secondary coil results in three different quality factors [23], [50], [51]. The first one Q_{2v} is the conventional loaded quality factor of the standard parallel *RLC* network. The second quality factor that may be defined is known as the current boost quality factor:

$$Q_{2i} = \frac{I_2}{I_{Sc}}. \tag{14}$$

Q_{2i} is used to quantify the increase in I_2 from its uncompensated value, I_{sc}, to its compensated value, $Q_{2i} \times I_{\mathrm{sc}}$. The amount of partial series compensation that may be carried out as quantified by Q_{2i} has been reported as being limited to less than 3 because of the added sensitivity to the overall resonance tuning of the secondary (i.e., due to component aging), as well as because of saturation of the pick-up coil ferrite that results from the increased flux density [50], [51].

The third quality factor that may be defined is the secondary's overall quality factor, which takes into account the effect of both Q_{2i} and Q_{2v}; this later quality factor is defined as

$$Q_{2t} = Q_{2v} \times Q_{2i}. \tag{15}$$

For practical designs, Q_{2t} is limited to being less than 10 [4], [47], and for most high-power EV charging systems it is less than 6. This limitation in the overall secondary Q is due to the challenges that arise in controlling the system because of the narrower bandwidth at higher values of Q_{2t}. Another factor that dictates the limit imposed on Q_{2t} is the need to maintain the secondary's VA ratings within the limits prescribed by governing safety standards such as UL [1], [23], [52].

With the aforesaid definitions in mind, $L_{2\mathrm{eq}}$ may also be expressed in terms of the three quality factors that result from the application of partial series compensation as

$$L_{2\mathrm{eq}} = \frac{R_{\mathrm{eq}}}{\omega Q_{2v}} = \frac{R_{\mathrm{eq}} Q_{2i}}{\omega Q_{2t}}. \tag{16}$$

III. Magnetic Pad Design and Characterization

The first step in the design of an IPT system is the selection of a suitable inductive structure geometry from a number of available choices [4], [11], [12]. Once a geometry that best suits the target application has been selected, a thorough FEA-based EM optimization of the design is undertaken prior to fabricating it. The goals of the FEA optimization are [51], [52], [57]–[61]:

1) achieving the highest possible values of mutual inductance and magnetic coupling over the system's target range of positional operation;
2) reducing the design's physical size and material cost as much as possible without compromising its power transfer capabilities;
3) achieving self-inductance values that will ensure coil voltage levels that are within established UL safety regulations;
4) ensuring regulatory compliance with established field emission standards (ICNIRP);
5) having a complete understanding of how all key magnetic attributes vary over the system's range of positional operation so as to properly design the primary and secondary power electronics in terms of component ratings and closed-loop control.

TABLE I
Nominal Magnetic Pad Attributes

Attribute Name	Value/Dimension/Material
Inductance (L_{avg})	170.51 μH
Quality Factor (Q_u)	535.67
AC Resistance (R_{AC})	60 mΩ
Power Loss (P_{loss})	94.61 W
Number of Turns (N)	22
Outer Diameter (O.D.)	482.6 mm
Inner Diameter (I.D.)	101.6 mm
Pitch (p)	3 mm
Conductor Diameter (d)	5.84 mm
Ferrite Length (F_L)	200 mm
Ferrite Width/Height (F_W , F_H)	25 mm
Ferrite Excess Length (F_E)	26.58 mm
Aluminum Shield Thickness (T)	6.5 mm
Former Dimensions (L, T)	540, 20 mm
Litz Conductor	Type II (16AWG 4×5X24/36)
Ferrite Material	Ferroxcube 3C94
No. of Ferrite Spokes	12

Because the focus of this paper was the design of the primary-side power electronics, the approach taken in the design of the magnetic pads was to forgo the initial FEA optimization process and instead construct the pads so as to replicate some of the better designs showcased in the literature, to this end, a circular Archimedean coil geometry was chosen [52], [57], [58]. Despite having lower coupling than other similarly sized coil geometries over identical air gaps and misalignment, for static EV charging applications, the circular geometry is still the most widely used [10].

The coils were designed so as to have known initial self-inductances of 125 μH with the aid Wheeler's formula for air-core Archimedean coils [62]. This initial value served only as a baseline, as it would later increase due to the addition of ferrite spokes. To act as a shield and enhance the mechanical attributes of the design, an aluminum backplane was added behind the ferrite spokes, effectively sandwiching the spokes between the polycarbonate coil former and the aluminum backplane [52].

The nominal attributes of the coils built are listed in Table I. All physical dimensions are defined in Fig. 2(a). The ac power loss of the pad as a result of skin effect is defined by (17), where I and V are the nominal operating primary and secondary pad voltage and current at rated power, and Q_u is the coil's unloaded quality factor defined with respect to its ac resistance at the target operating frequency

$$P_{\mathrm{loss}} = \frac{I_1 V_1 + I_2 V_2}{Q_u}. \tag{17}$$

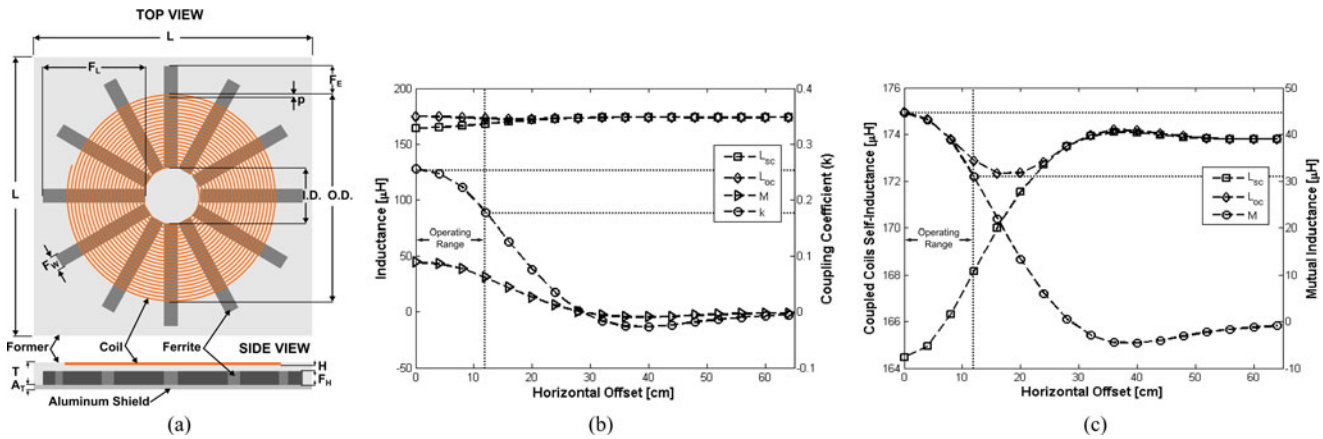

Fig. 2. Mechanical features and measured coupled magnetic pad attributes at a 16-cm vertical offset: (a) Magnetic pad construction; (b) coupling coefficient, mutual inductance, short- and open-circuit self-inductance; (c) expanded view of mutual- and self-inductances.

Once the coils were built their magnetic attributes were experimentally measured and used to carry out the design of the primary- and secondary-side power electronics. For precise measurement of the pads' coupled self- and mutual-inductances, as well as coupling coefficient over their range of positional operation, the test bench shown in Fig. 4(c) was built. To measure M and k, the coupled pad's were energized with a known primary current by means of an inverter with a series resonant capacitor. The required measurements were taken, while the pads were misaligned in the vertical and/or horizontal directions in small steps.

The coupled-coil self-inductances were measured at each point along the horizontal offset trajectory with an *LCR* meter. The mutual inductance was obtained by measuring the secondary's open-circuit voltage $V_{L2\mathrm{oc}}$ and the primary's current I_1. The coupling coefficient was obtained by two separate methods. The first method applied was the measurement of the primary-coil voltage V_{L1} and $V_{L2\mathrm{oc}}$ so as to use the voltage transfer ratio $V_{L2\mathrm{oc}}/V_{L1}$ as a measure of k [39]. The second method used was the use of the conventional ac circuit definition of k given as the ratio of M and the square root of the product of the coupled self-inductances. Both methods produced very similar results. Fig. 2 shows the pads measured magnetic attributes over a range of axial misalignment spanning 64 cm for a coil-to-coil separation distance of 16 cm. Fig. 2(b) shows all pad attributes together, while Fig. 2(c) shows an expanded view of the mutual and self-inductances only. As can be seen, the coupled self-inductances were measured for two different conditions: 1) a shorted secondary pad (L_{sc}), and 2) an open secondary pad (L_{oc}). The measurements are taken with the *LCR* meter on one pad, while the other one coupled to it has its terminals either shorted or opened. Consideration of these two cases is necessary because depending on the resonant topology chosen for the primary and secondary matching networks, the self-inductance may behave differently. For example, for the parallel resonant topology, the pad's self-inductance varies according to the short-circuit measurement profile, while for the series resonant topology, the inductance varies according to the open-circuit measurement profile [45]. The plots of mutual inductance and coupling verify the existence of a fixed characteristic null in the magnetic profile of circular coils [52]. Another noteworthy observation is that L_{sc} and L_{oc} both converge to a common value as the pads are decoupled, with the convergence starting around the characteristic null point. As already noted, the operating range of coupling is a crucial design variable that must be known in order to properly design the power supply, this in fact is one of they key items that will be standardized by the J2954 task force for interoperability [33]. Fig. 2 shows the operating range of coupling being considered for this comparative study, namely the region to the left of the vertical dashed line inclusive. This range corresponds to a maximum axial misalignment distance of 12 cm, which translates to a coupling coefficient in the neighborhood of 0.18–0.25.

IV. Power Supply Architectures

A. SLC Resonant Power Supply

Fig. 3(a) shows the simplified equivalent circuit of the SLC power supply with all energy storage elements assumed to be lossless [45]. As can be seen, the ECN of the SLC architecture is made up of a single capacitor in series with the primary coil

$$C_1 = \frac{L_{2\mathrm{eq}}}{\omega_0^2\left[L_{\Delta 1}L_{2\mathrm{eq}} - M^2\right]} \tag{18}$$

$$L_{\Delta 1} = L_1 - L_{1\mathrm{eq}}. \tag{19}$$

The value of the tuning capacitor C_1 is sized according to (18) so that when the system is operated at its target frequency, the resulting equivalent primary inductance $L_{1\mathrm{eq}}$ seen by the FB is about 10% of L_1 [14]. This partial series compensation scheme is equivalent to choosing C_1 so as to fully resonate with L_1 at $f_0 = \frac{1}{2\pi\sqrt{L_1 C_1}}$, and then, operating the system at a frequency $f_0' = 1.05 \times f_0$ [63].

The reason why the SLC power supply is operated slightly (5%) above perfect resonance is that this allows for the reduction of switching power losses in the FB semiconductors by means of the circulating inductive energy associated with the residual inductance $L_{1\mathrm{eq}}$ positioning zero voltage across the

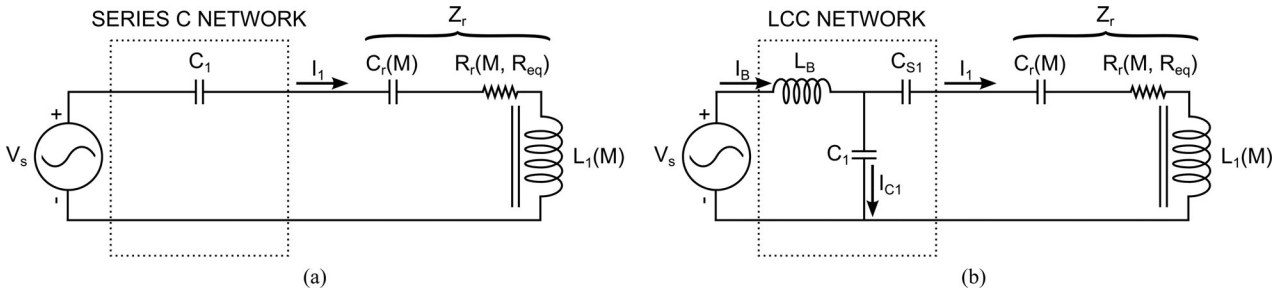

Fig. 3. Simplified ac equivalent circuit of primary power supply architectures being compared: (a) SLC architecture, and (b) *LCL* architecture.

semiconductors in each leg of the FB just before turn-on. This placement of zero voltage across the switches reduces the instantaneous turn-on loss that is normally associated with the finite period of time during which the drain-to-source voltage $V_{\rm DS}$ of the nonideal switch is decreasing, while its drain current I_D is rising. This mode of operation is commonly known as zero voltage switching (ZVS), and the specific mechanism used to reduce $V_{\rm DS}$ to zero is the complete discharge of the parasitic drain-to-source capacitance of the switch $C_{\rm DS}$ by means of current flowing through $L_{1\rm eq}$ and the free-wheeling body diode of the MOSFET during the dead-time, t_d, that occurs between the turn-off and turn-on of series switches.

The sizing of C_1, also takes into account the nominal value of $C_r(M)$ at the system's target operating frequency and coupling point; accordingly, C_1 is chosen so that the equivalent capacitance resulting from the combination of $C_r(M_0)$ and C_1 will yield the desired ZVS mode of operation previously described. If the system deviates significantly away from its nominal operating range of coupling, then the resulting variation in the equivalent series tuning capacitance and the nonlinear change in L_1 described in Section III will take the FB out of the desired ZVS mode and the power losses will increase significantly [40]. To prevent the foregoing situation and a potential failure of the semiconductors, the system's switching frequency must be adjusted so as to always maintain ZVS operation. As discussed in [64], the frequency control scheme cannot rely on an autonomous phase-locked loop-based approach due to bifurcations that are inherent in the system because of its high order. Instead, a few discrete points in the frequency spectrum around the nominal operating frequency are selected and used to ensure the desired ZVS operating mode. The SLC architecture is attractive primarily because of its very simple matching network, consisting of only a single capacitor, which tends to result in a reduced physical implementation cost and complexity. Despite its reduced component count, the need to dynamically vary the switching frequency of the SLC topology adds to the complexity of the closed-loop controller design. In addition, the effective impedance seen by the FB is very sensitive to changes in both coupling and loading, which further increases the complexity of the controller. The foregoing sensitivity can also result in a very large current stress on the bridge semiconductors when the coupling of the magnetic pads decreases significantly beyond its intended operating range [39], [65].

When C_1 is chosen according to the previously described procedure, the value of the primary current is given as follows:

$$I_1 = \frac{V_S}{|R_r + j\omega_0 L_{1\rm eq}|} = \frac{2\sqrt{2}V_{\rm DC}}{\pi|R_r + j\omega_0 L_{1\rm eq}|}\sin\left(\frac{\omega_0 \times t_{\rm PS}}{2}\right) \tag{20}$$

using (20) along with (13) the design of the SLC topology can be finalized by determining either the required dc-bus voltage $V_{\rm DC}$ or the required HF isolation transformer turns ratio needed to achieve the target I_1. Selection of $V_{\rm DC}$ assumes that the dc-bus voltage can be controlled at will, such as would be the case if the system had an intermediate buck or boost converter stage between the utility input and the FB. On the other hand, selection of a suitable HF transformer turns ratio assumes that the dc-bus voltage is limited.

B. Series–Parallel Resonant (LCL) Power Supply

Fig. 3(b) shows the simplified equivalent circuit of the *LCL* power supply neglecting all parasitic resistances. As can be seen, the ECN of the *LCL* architecture has two more discrete energy storage elements than the SLC topology, namely the series bridge inductance L_B and the series capacitance C_{S1}. Moreover, the primary resonant capacitance C_1 is now in parallel with the primary coil and C_{S1}. This topology is sometimes also referred to as an *LCL*-T topology because of the characteristic T-shape of the ECN. The series capacitance C_{S1} is used for partial series compensation of L_1 so as to reduce it to a smaller equivalent value $L_{1\rm eq}$. The parallel capacitance C_1 is chosen so as to fully resonate with $L_{1\rm eq}$ at the system's operating frequency. The bridge inductance is used to convert the HF voltage source characteristic of the FB to an equivalent current source, and for this reason, this ECN is sometimes spoken of as being an impedance conversion network (ICN) [35], [37].

A very desirable characteristic of the *LCL* power supply is that when operated at or very close to resonance, it behaves as a constant current source over a very large range of coupling and loading making its control loop design easier [66]. This is in contrast with the SLC topology, which is quite sensitive to changes in coupling and loading and requires a combination of dc-bus voltage and frequency adjustments to maintain its constant current source operation [1].

The primary current of the *LCL* topology is fixed by the effective reactance X_1 of the primary coil along with its partial

series tuning capacitor and is given as

$$I_1 = \frac{V_S}{X_1} = \frac{2\sqrt{2}V_{\mathrm{DC}}}{\pi X_1}\sin\left(\frac{\omega_0 \times t_{\mathrm{PS}}}{2}\right). \tag{21}$$

Another feature of the *LCL* architecture that is often praised in the literature is that it reduces the current stress of the bridge semiconductors by constraining the large reactive resonant currents to flow only in the resonant tank [23]. The FB only sources the current associated with the active power flow and the resonant tank losses. The decrease of the bridge current results in a reduced on-time conduction loss for the semiconductors.

The strategy in designing the *LCL* network is to size the energy storage elements so that the magnitude of all the resulting reactances are equal. Accordingly, the design equations that govern the sizing of the *LCL* network are as follows:

$$C_{S1} = \frac{L_{2\mathrm{eq}}}{\omega_0^2\left[L_{\Delta 1}L_{2\mathrm{eq}} - M^2\right]} \tag{22}$$

where $L_{\Delta 1}$ is once again given by

$$L_{\Delta 1} = L_1 - L_{1\mathrm{eq}} \tag{23}$$

and $L_{1\mathrm{eq}}$ is once again the equivalent inductance of the partially tuned primary coil

$$L_{1\mathrm{eq}} = \frac{X_1}{\omega_0}. \tag{24}$$

The parallel resonant tuning capacitance C_1 is obtained from

$$C_1 = \frac{1}{\omega^2 L_{1\mathrm{eq}}}. \tag{25}$$

Finally, the bridge inductance is in practice set to be 10% larger than the value of $L_{1\mathrm{eq}}$, so as to ensure that the inverter will always see a lagging/inductive load [37]

$$L_B = 1.1 \times L_{1\mathrm{eq}}. \tag{26}$$

A lagging load is desirable because if the bridge were to ever become capacitively loaded, then the semiconductor losses would increase significantly due to large reverse recovery currents in the semiconductor's intrinsic body diode [51]. Moreover, as noted in [66], the power stage can be operated in a ZVS mode provided that the chosen switching control scheme ensures conduction in the intrinsic body diodes prior to switch turn-on. This operating mode coupled with the previously noted reduced current stress during conduction can result in very high converter efficiency.

As was the case with the SLC design strategy, the selection of the capacitance C_{S1} takes into account the reflected virtual capacitance $C_r(M_0)$ [23]. The bridge inductance L_B could be implemented with an actual inductor, but by designing the HF transformer so as to have a precise value of an overall equivalent leakage inductance, it can be constructively used as a part of the matching network, resulting in a reduced number of components.

TABLE II
NOMINAL DESIGN SPECIFICATIONS

Specification Name	Specification Value
P_{max}	3 kW
Eff_{min}	85%
f_0	30 kHz
Secondary Topology	parallel–series
k_{min}	0.1773
$M(k_{\mathrm{min}})$	30.93 μH
$L_{2\mathrm{sc}}(k_{\mathrm{min}})$	168.15 μH
$L_{1\mathrm{sc}}(k_{\mathrm{min}})$	168.15 μH
$L_{1oc}(k_{\mathrm{min}})$	172.87 μH
C_{s2}	0.23 μF
C_2	0.64 μF
R_{eq}	17.76 Ω
Q_{2t}	3
Q_{2v}	2.14
Q_{2i}	1.40
V_{DC_0}	240 V

V. OVERALL SYSTEM DESIGN METHODOLOGY AND PHYSICAL IMPLEMENTATION

The design of the primary power supply requires that the following parameters be known:

1) maximum power transfer level P_{max};
2) nominal operating frequency f_0;
3) magnetic pad characteristics: k_{min}, $M(k_{\mathrm{min}})$, $L_{\mathrm{sc}}(k_{\mathrm{min}})$, and $L_{oc}(k_{\mathrm{min}})$;
4) secondary-side ECN topology and energy storage element values;
5) nominal load value R_{eq};
6) nominal value of the three secondary quality factors: Q_{2t}, Q_{2v}, and Q_{2i};
7) the nominal dc-bus input voltage of the inverter V_{DC_0}.

For this study, the above stated specifications are shown in Table II. The power level was selected so as to operate close to an SAE level II charging power. The nominal operating frequency was set at 30 kHz primarily because at the time when the magnetic pads for this study were initially designed most of the research on wireless charging was focused on frequencies around 20 kHz. Recently, the J2954 charging task force set the nominal operating frequency for light duty vehicles at 85 kHz [33], however, because of the limitations imposed by the large resonant voltages in the matching networks of the constructed coils at higher frequencies and because of limitations imposed by the value of capacitors that were available to complete the physical implementation, the final frequency used to drive the system and carry out the comparison was actually 29 kHz.

The nominal dc bus voltage was chosen so as to have a range of regulation voltages that would allow for both architectures to deliver the target power over the full operating range of coupling and loading being considered as well as to readily highlight the differences in the voltage regulation strategy needed for each architecture. In a practical setting, a higher nominal dc bus voltage would likely be chosen for the *LCL* topology.

For this particular design, the extreme operating point is chosen to correspond to a maximum coil-to-coil air gap of 16 cm and an axial misalignment of 12 cm. This operating point

TABLE III
POWER SUPPLY MATCHING NETWORK VALUES

	L_B	C_1	C_{S1}
SLC	N/A	0.21 μF	N/A
LCL	49.25 μH	0.63 μF	0.28 μF

corresponds to $k_{\min}$ shown in Table II and was selected so as to be representative of the nominal light duty EV ground clearance and the ongoing research efforts showcased in the literature for static wireless charging [23], [41], [44]. The magnetic design characteristics for the full operating range of coupling are shown in Fig. 2. As noted in Section III, the region to the left of the dashed vertical line is the full operating range of coupling. The idea is to ensure that the system is able to transfer the required power at the boundary, with the understanding that if it is able to do so, then it will also be able to do so at higher coupling points in the operating range. In a practical implementation, a feedback control system would be used to guide the user in parking so as to ensure operation within the target nominal range of coupling as well as to disable operation altogether when outside it [23].

From the given specifications, the primary current needed to transfer the required power can be computed using (13); the calculated value serves as an initial design reference value. The final value of I_1 for the physical implementation may need to be larger in order to transfer the target power level. The need to increase the primary current upon completion and evaluation of the initial physical implementation is well reported upon in the literature [4], [13], [38], [52]. As highlighted in the cited references, the VA of the tuned secondary must be able to support the desired power transfer level.

Next, the values of the energy storage elements in the matching network of each power supply architecture are obtained by application of the governing equations presented in Section IV. The actual values used for the physical implementation are listed in Table III. Once the component values on both the primary and secondary have been obtained, their respective voltage and current ratings must be determined so as to ensure their safe operation. The equations governing the ratings of the primary- and secondary-side elements are summarized in Appendix A in terms of RMS values.

As is seen from the complete mathematical model presented thus far, the voltages and currents will vary with changes in coupling and loading. Consequently, the establishment of the peak ratings requires that all of the system's equations be swept over their full range of coupling and loading and that the maximum values of each element's voltage and current be ascertained. This task is made even more challenging because as noted in Section III, when the coupling changes, so do the mutual- and self-inductances of the coupled coils. To be able to tackle the said computationally intensive task, a MATLAB routine was developed that steps through the system's range of coupling and loading. For the coupling sweep, the routine evaluates each expression in the model with the corresponding measured values of mutual- and self-inductance at the given coupling point for a fixed load value. In like manner, the routine also evaluates all expressions at a fixed coupling point, while varying the load over the desired range. The resulting voltage and current ratings for both sweeps are stored in two result arrays, one for the coupling sweep and another for the loading sweep. The routine then compares the peak ratings of both result arrays for each circuit element and extracts the maximum values. In addition to determining peak component ratings, the theoretical losses and efficiency of the designed system may also be obtained over its operating range with the foregoing MATLAB routine by inclusion of the measured parasitic resistances of the energy storage elements and of the nominal $R_{\text{ds(on)}}$ of the semiconductors used. Much as was the case with I_1, the max ratings, losses, and efficiency obtained from sweeping the theoretical model serve only as an initial reference for the design, and may have to be adjusted upon evaluation of the physical system's behavior in the face of higher order effects associated with component drift do to prolonged operation.

Fig. 4 shows the physical implementation of the complete IPT system designed for this study and the operating waveforms for each power supply as well as for the vehicle side pick-up. Fig. 4(a) is the series resonant architecture, while Fig. 4(b) is the *LCL* architecture. Fig. 4(c) shows the entire IPT system operating a rated conditions. The 3-kW resistive load was implemented with a 3-by-3 array of light bulbs consisting of three parallel connected branches, each with three series connected bulbs. Each bulb in the array was rated for 1 kW at 120 V. The core of the HF isolation transformer (HF XFRMR) between the bridge and the ECN was implemented with the same ferrite material used for the spokes of the magnetic pads. The constructed transformer had a one-to-one turns ratio with 21 turns per side. Moreover, its effective leakage inductance was controlled by adjusting the core's air gap length until it measured 67.28 μH. For the SLC topology, the transformer's leakage inductance was completely canceled by setting C_B equal to 0.4 μF, whereas for the *LCL* topology it was reduced to the target value of L_B by setting C_B equal to 1.56 μF. For the FB switching network, the IXFN132N50P3 power MOSFET was chosen because of its very low $R_{\text{ds(on)}}$, fast intrinsic body diode, and low gate charge requirement. The gate driver stage was implemented with two low-cost FAN7390 bootstrap gate driver IC's, and the control logic was generated using a TMS320F28335 DSP from Texas Instruments. All PCB's are double sided and were fabricated in-house using a QC5000 prototyping system. The gate driver stage was implemented on a separate PCB than the power stage so as to ensure good signal integrity with the limited number of copper layers used [22]. In the operating waveforms, V_{INV} is the inverter output voltage, and it leads the inverter current by 36° for both architectures confirming the desired inductive mode of operation targeted in the design. V_{GS} is the gate-to-source voltage of one of the power switches. V_{L1} is the primary coil voltage, and the 86.53 MHz ringing apparent on it at the switching instants is a result of the transformer's parasitics resonating with the HF components of V_{INV}. The stated root cause of the ringing was confirmed by two separate tests: First, the transformer was completely removed, leaving only the ECN's, in which case the ringing disappeared completely; second, when the value of the transformer's parasitic attributes were modified by either

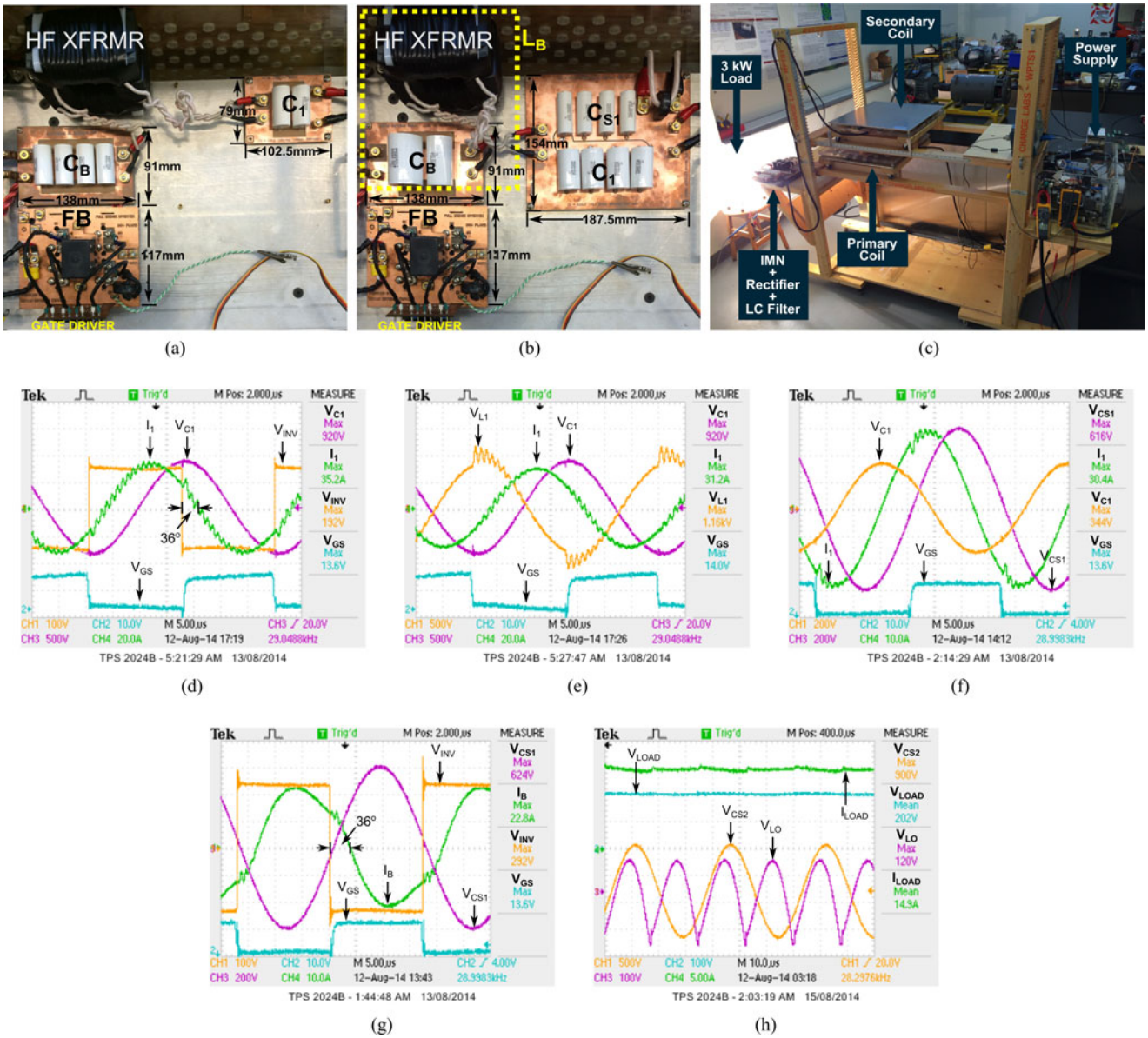

Fig. 4. System implementation and operating waveforms: (a) SLC power supply, (b) *LCL* power supply, (c) complete system operating at rated load and minimum coupling, (d)and (e) SLC waveforms, (f) and (g) *LCL* waveforms, (h) secondary-side waveforms.

changing the core's air-gap length or the number of turns, the frequency of the ringing would also change. A practical way to eliminate the HF ringing is to place a split and balanced inductor between the bridge output and the transformer so as to filter as much harmonic content as possible. All of the operating waveforms were captured from the complete set-up shown in Fig. 4(c); consequently, V_{LOAD} and I_{LOAD} in Fig. 4(h) are the voltage and current of the 3-kW light-bulb load bank. Video of the full working system for both power supply architectures may be viewed online via the hyperlinks in Appendix B.

VI. Performance Comparison

A. Size and Complexity

The SLC topology has the lowest number of discrete energy storage elements, with only one tuning capacitor C_1. On the other hand, the *LCL* architecture requires the use of two more energy storage elements, but by constructively using the parasitic inductance of the common HF isolation transformer, the total component count for the *LCL* power supply is reduced to just two, namely: C_{S1} and C_1. In view of the higher component count, the *LCL* topology is more complex in its physical implementation and its volumetric space requirements.

Fig. 5(c) shows the normalized open-loop power of each power supply as a function of coupling. The constant current source characteristic of the *LCL* architecture is clearly in evidence. On the other hand, the sensitive nature of the SLC topology to changes in coupling is seen in the fact that as the coupling increases, the power actually decreases. This later behavior is counterintuitive, but it is readily explained by the fact that the SLC's primary current is heavily affected by the variation of the reflected secondary load. Fig. 5(d) shows the open-loop primary

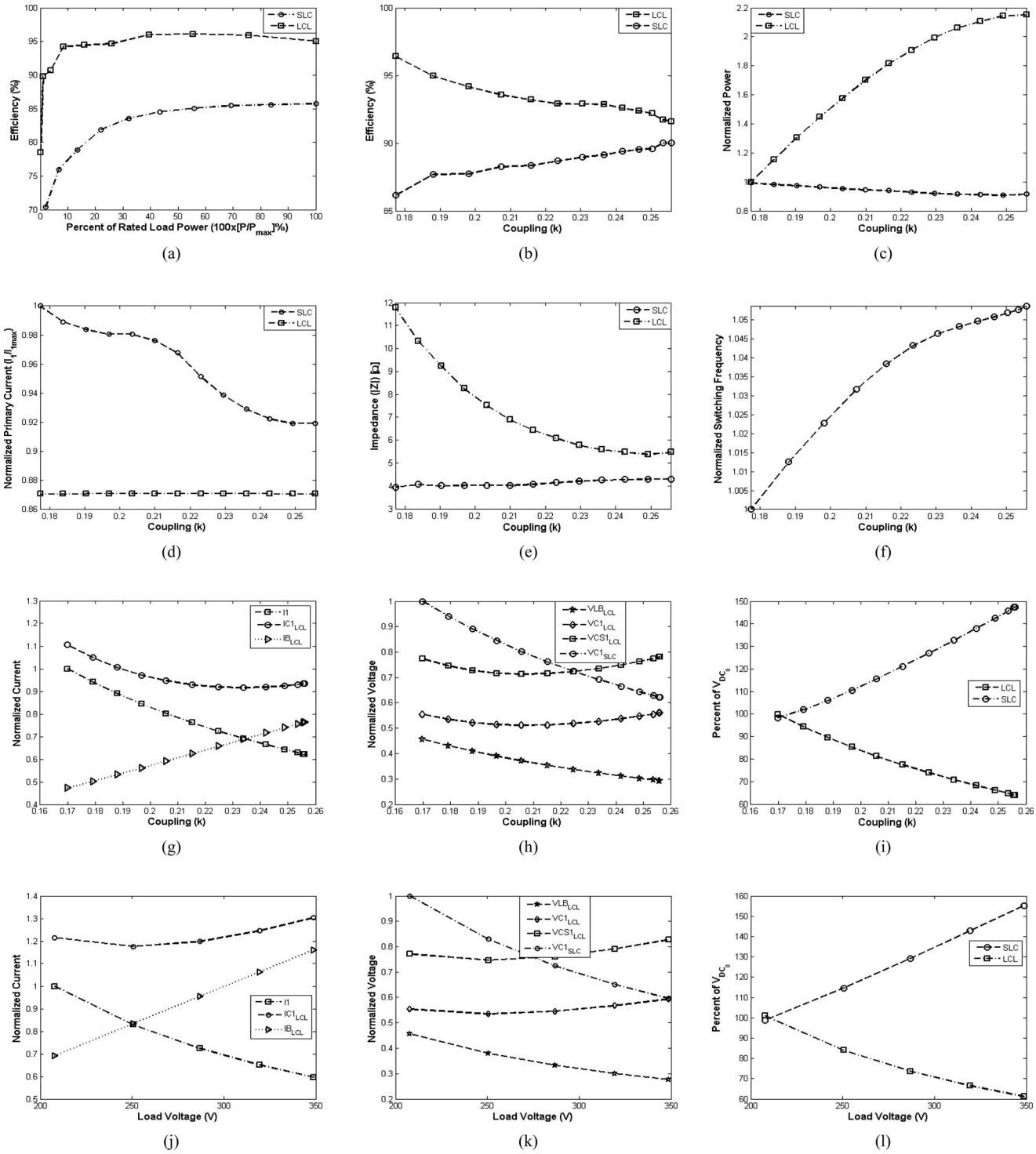

Fig. 5. Measured performance of SLC and *LCL* power supplies: (a) Efficiency versus percent of rated load, (b) efficiency versus coupling under constant power, (c) open-loop normalized power versus coupling, (d) open-loop normalized primary current versus coupling, (e) ECN impedance magnitude versus coupling, (f) SLC switching frequency for sustained ZVS operation over range of coupling (normalized to the nominal f_0), (g) normalized ECN currents versus coupling under constant power (normalized to the peak value of I_1), (h) normalized ECN voltages versus coupling under constant power (normalized to the peak value of $V_{C1_{\rm SLC}}$), (i) normalized dc bus voltage versus coupling for constant power (normalized to $V_{\rm DC_0}$), (j) normalized ECN currents versus load voltage under constant power (normalized to the peak value of I_1), (k) normalized ECN voltages versus coupling under constant power (normalized to the peak value of $V_{C1_{\rm SLC}}$), (l) normalized dc bus voltage versus load voltage for constant power (normalized to $V_{\rm DC_0}$).

current for each topology as a function of coupling. As expected, the *LCL* topology has a perfectly constant current throughout the entire range of coupling, while the SLC topology's current decreases significantly as coupling increases. As can been seen in Fig. 5(e), as the coupling increases, the reflected impedance seen by the SLC architecture increases correspondingly; thereby, reducing the initial primary current from its nominal value. This sensitivity requires that the dc-bus voltage be increased so as to maintain a constant current source operating mode.

An increase in R_L beyond its nominal operating point would translate to an increase in Q_{2v} in (11). For the *LCL* topology, with its constant current characteristic, such a condition would result in an increase in the open-loop power sourced by the power supply accompanied by a corresponding rise in the inverter current. In practice, however, the closed-loop controller would act to lower the dc-bus voltage so as to maintain the desired power level with a smaller primary current. On the other hand, for the SLC topology the same deviation in R_L would result in a decrease in the open-loop power delivered due to the decrease of the primary current caused by the larger reflected secondary impedance. In the latter case, the increase in Q_{2v} is not enough to overcome the simultaneous reduction in the primary current due to the square dependence of the power on I_1. So for the SLC topology, the controller would have to increase the dc-bus voltage so as to maintain the desired power level with the higher value of Q_{2v}.

Given the target range of coupling chosen for this study, it was determined that the FB switching frequency for the SLC architecture would have to be adjusted according to the characteristic shown in Fig. 5(f) so as to maintain ZVS. This requirement along with the need to vary the dc-bus voltage so as to regulate the primary current against changes in coupling make the overall control of the SLC architecture more complex.

B. Cost and Component Stress

The cost of a power supply is defined as the ratio of total active power delivered to the load and the total VA rating of the supply. As noted in [45], the VA stored in the tuning components of the power supply is related to its size and associated cost. Hence, the ratio of kW/kVA is a good estimate of the kW/$ of the power supply. In this regard, the cost of the SLC and *LCL* power supplies when operated at their rated power levels are 0.041 and 0.042, respectively. So as might be expected, the *LCL* topology has a higher overall cost, though not by much (i.e., 2.41%).

Fig. 5(g) and (j) shows the normalized voltages across all energy storage elements, for both architectures, over the full operating range with the normalization done with respect to the voltage of the SLC series capacitor. As can be observed, the voltage stress on the single capacitor of the SLC topology is much higher than that on any of the capacitors of the *LCL* topology over the full operating range. This fact is further corroborated in Fig. 4(c), which shows a 920-V stress on the series capacitor of the SLC topology, and a 624-V stress on the series capacitor of the *LCL* topology. Another factor that causes a higher stress on the components of the SLC topology is the fact that at rated conditions, the entire primary current, in this case 30 A, is handled by the semiconductors in its switching network, compared to only 23 A for the FB of the *LCL* topology. This fact makes the required current and power rating of the switching devices for the SLC topology 1.3 and 1.7 times greater, respectively, than those for the *LCL* topology for the same power transfer level; moreover, as will be explained next this later factor also plays an important role in efficiency of each architecture.

C. Efficiency

Fig. 5(a) and (b) shows the end-to-end efficiency of the complete IPT system for both architectures as a function of the percent of rated loading and coupling, respectively. The foregoing efficiency is defined as the ratio of the power at the load and the input power at the dc bus of the switching network. Moreover, the efficiency of Fig. 5(b) was measured, while the load power was maintained constant over the full range of coupling via the regulation of the dc-bus voltage according to the characteristic shown in Fig. 5(i). For this study, the losses in the FB were measured using the TPS2PWR1 power analysis application software for the Tektronix TPS2024B oscilloscope. In the case of the SLC topology, the bridge losses at full power were 394 W, whereas for the *LCL* topology they were only 15 W. This translates to an 88.72% and 99.52% efficiency for the power stage of the SLC and *LCL* architectures, respectively. A noteworthy observation in Fig. 5(b) is that as the coupling changes, the efficiency of the *LCL* architecture decreases from its peak value to just above 91%, while that of the SLC architecture increases to 90%. This happens because as seen in Fig. 5(h), as the coupling increases, the bridge current sourced by the *LCL* increases resulting in increased semiconductor losses, whereas for the SLC the opposite takes place.

The power supply's light load efficiency is a very important figure of merit in EV charging applications because the power supply is fully loaded for only one third of the total charging time, namely during the bulk charging stage. However, during the absorption and float stages, which account for two thirds of the total charging time, the power supply is only partially loaded [67]. As is seen in Fig. 5(a), the *LCL* architecture has better light-load performance than the SLC, this is so because as highlighted in [65], [66], under no load, the input impedance of the *LCL* network becomes infinite; consequently, the inverter output current becomes zero and the converter is able to maintain very high light-load efficiency. In contrast, at light loads, the SLC topology sources very large reactive currents due to the very small tuned impedance seen by the inverter [39]. A way to improve the light-load efficiency of the SLC topology is to have a secondary-side regulator [42], but this improvement comes at the expense of an increased cost and complexity on the vehicle side.

As can be seen from these results, the *LCL* topology is clearly superior over the entire range of loading and coupling, achieving a peak end-to-end efficiency of 96%, and maintaining an overall higher efficiency even at its worst case efficiency operating point. The SLC topology, on the other hand, suffers from poorlight-load efficiency, dropping to as low as 70% at light

TABLE IV
SUMMARY OF A COMPARATIVE STUDY

	Number of Capacitors	Capacitor Voltage Stress	Cost [W/VA]	Control Complexity	Rated Load Efficiency	Light Load Efficiency
SLC	1	HIGH	0.041	HIGH	86%	76%
LCL	2	LOW	0.042	LOW	96%	95%

load. Furthermore, the peak system efficiency at the nominal operating point with the SLC supply is only 86%. This 10% difference in the peak efficiency of the two architectures is a result of the fact that the bridge power switches of the SLC topology must handle the full-resonant current, which increases the semiconductor loses even despite the sustained ZVS operation. On the other hand, the *LCL* topology is able to maintain very high efficiency because the bridge stage only handles the current associated with the active power transfer and the resonant tank losses. The foregoing results are still applicable at 85 kHz because the key reason for the higher efficiency of the *LCL*, namely the lower current stress of the semiconductors, is independent of frequency; consequently, while it is to be expected that the overall efficiency of both topologies would go down at 85 kHz due to the increased switching losses, the efficiency of the *LCL* would still remain higher than that of the SLC.

VII. CONCLUSION

The development of wireless EV charging technologies has gained unparalleled momentum over the latter half of the past decade. The release of a formal industry standard governing this novel technology will enable OEM's to bring wireless EVs to market as early as 2016. A key question that remained unanswered until now was: Which of the two power supply architectures commonly used in wireless EV chargers is better in terms of size, complexity, cost, and efficiency?

This paper has compared the foregoing two topologies by applying an identical performance test. The results, which are summarized in Table IV, show that while the SLC topology has slightly lower component count and cost, the *LCL* topology is superior in terms of its power conversion efficiency over the full range of coupling and loading imposed. Moreover, its constant current source characteristic make its closed-loop control implementation easier than the alternative SLC architecture. Because the efficiency of the power supply is a key figure of merit in a wireless EV charging, the results presented in this study point to the likely adoption of the *LCL* topology for a future standardized implementation of wireless EV charging.

APPENDIX A
SYSTEM RMS VOLTAGES AND CURRENTS

A. LCL Architecture

$$I_B = \frac{(1-\omega^2 L_{1\mathrm{eq}}C_1)+j\omega C_1 R_r}{R_r(1-\omega^2 L_B C_1)+j\omega[L_B(1-\omega^2 L_{1\mathrm{eq}}C_1)+L_{1\mathrm{eq}}]}V_S \quad (27)$$

$$I_{C1} = \frac{(1-\omega^2 L_{1\mathrm{eq}}C_1)+j\omega C_1 R_r - 1}{R_r(1-\omega^2 L_B C_1)+j\omega[L_B(1-\omega^2 L_{1\mathrm{eq}}C_1)+L_{1\mathrm{eq}}]}V_S \quad (28)$$

$$I_1 = \frac{1}{R_r(1-\omega^2 L_B C_1)+j\omega[L_B(1-\omega^2 L_{1\mathrm{eq}}C_1)+L_{1\mathrm{eq}}]}V_S \quad (29)$$

$$V_B = \frac{j\omega L_B[(1-\omega^2 L_{1\mathrm{eq}}C_1)+j\omega C_1 R_r]}{R_r(1-\omega^2 L_B C_1)+j\omega[L_B(1-\omega^2 L_{1\mathrm{eq}}C_1)+L_{1\mathrm{eq}}]}V_S \quad (30)$$

$$V_{C1} = \frac{[(1-\omega^2 L_{1\mathrm{eq}}C_1)+j\omega C_1 R_r - 1]V_S}{j\omega C_1(R_r(1-\omega^2 L_B C_1)+j\omega[L_B(1-\omega^2 L_{1\mathrm{eq}}C_1)+L_{1\mathrm{eq}}])} \quad (31)$$

$$V_{CS1} = \frac{V_S}{j\omega C_{S1}(R_r(1-\omega^2 L_B C_1)+j\omega[L_B(1-\omega^2 L_{1\mathrm{eq}}C_1)+L_{1\mathrm{eq}}])} \quad (32)$$

$$V_{CS1} = \frac{V_S}{j\omega C_{S1}(R_r(1-\omega^2 L_B C_1)+j\omega[L_B(1-\omega^2 L_{1\mathrm{eq}}C_1)+L_{1\mathrm{eq}}])} \quad (33)$$

$$L_{1\mathrm{eq}} = L_1 - \frac{1}{\omega^2 C_{S1}} - \frac{1}{\omega^2 C_r\,(M, R_{\mathrm{eq}})}. \quad (34)$$

B. SLC Architecture

$$I_1 = \frac{V_S}{R_r + j\omega L_{1\mathrm{eq}}} \quad (35)$$

$$V_{C1} = \frac{V_S}{j\omega C_1[R_r + j\omega L_{1\mathrm{eq}}]} \quad (36)$$

$$V_{L1} = \frac{j\omega L_1 V_S}{R_r + j\omega L_{1\mathrm{eq}}} \quad (37)$$

$$L_{1\mathrm{eq}} = L_1 - \frac{1}{\omega^2 C_1} - \frac{1}{\omega^2 C_r\,(M, R_{\mathrm{eq}})}. \quad (38)$$

C. Secondary Side

$$I_2 = \frac{R_{\mathrm{eq}}}{j\omega L_{2\mathrm{eq}} + R_{\mathrm{eq}}(1-\omega^2 L_{2\mathrm{eq}}C_2)}\frac{MI_1}{L_{2\mathrm{eq}}} \quad (39)$$

$$I_{C2} = \frac{-R_{\rm eq}\omega^2 L_{2\rm eq} C_2}{j\omega L_{2\rm eq} + R_{\rm eq}(1-\omega^2 L_{2\rm eq} C_2)} \frac{MI_1}{L_{2\rm eq}} \quad (40)$$

$$V_{L2} = \frac{\omega R_{\rm eq} L_2}{\omega L_{2\rm eq} - jR_{\rm eq}(1-\omega^2 L_{2\rm eq} C_2)} \frac{MI_1}{L_{2\rm eq}} \quad (41)$$

$$V_{CS2} = \frac{-R_{\rm eq}}{\omega^2 L_{2\rm eq} C_{s2} - j\omega R_{\rm eq} C_{s2}(1-\omega^2 L_{2\rm eq} C_2)} \frac{MI_1}{L_{2\rm eq}} \quad (42)$$

$$V_{C2} = \frac{\omega R_{\rm eq} L_{2\rm eq}}{\omega L_{2\rm eq} - jR_{\rm eq}(1-\omega^2 L_{2\rm eq} C_2)} \frac{MI_1}{L_{2\rm eq}}. \quad (43)$$

APPENDIX B
ONLINE MULTIMEDIA OF A WORKING SYSTEM

A. SLC Architecture

https://www.youtube.com/watch?v=GNDM4SKEf90.

B. LCL Architecture

https://www.youtube.com/watch?v=wt_pU8H9GNU.

REFERENCES

[1] G. Covic and J. Boys, "Inductive power transfer," *Proc. IEEE*, vol. 101, no. 6, pp. 1276–1289, Jun. 2013.

[2] A. W. Green and J. T. Boys, "10 kHz inductively coupled power transfer-concept and control," in *Proc. 5th Int. Conf. Power Electron. Variable-Speed Drives*, Oct. 1994, pp. 694–699.

[3] G. A. Covic, G. Elliott, O. Stielau, R. M. Green, and J. T. Boys, "The design of a contact-less energy transfer system for a people mover system," in *Proc. Power Syst. Technol., Int. Conf.*, 2000, vol. 1, pp. 79–84.

[4] O. Stielau and G. A. Covic, "Design of loosely coupled inductive power transfer systems," in *Proc. Power Syst. Technol., Int. Conf.*, 2000, vol. 1, pp. 85–90.

[5] J. Boys and A. Green. (1994, Mar. 8). Inductive power distribution system. U.S. Patent 5 293 308. [Online]. Available: http://www.google.com/patents/US5293308

[6] C.-H. Hu, C.-M. Chen, Y.-S. Shiao, T.-J. Chan, and L.-R. Chen, "Development of a universal contactless charger for handheld devices," in *Proc. IEEE Ind. Electron., Int. Symp.*, Jun. 2008, pp. 99–104.

[7] S. Hui and W. C. Ho, "A new generation of universal contactless battery charging platform for portable consumer electronic equipment," in *Proc. IEEE 35th Annu. Power Electron. Spec. Conf.*, Jun. 2004, vol. 1, pp. 638–644.

[8] C.-G. Kim, D.-H. Seo, J.-S. You, J.-H. Park, and B.-H. Cho, "Design of a contactless battery charger for cellular phone," in *Proc. IEEE 15th Annu. Appl. Power Electron. Conf. Expo.*, 2000, vol. 2, pp. 769–773.

[9] A. Sample, D. Meyer, and J. Smith, "Analysis, experimental results, and range adaptation of magnetically coupled resonators for wireless power transfer," *IEEE Trans. Ind. Electron.*, vol. 58, no. 2, pp. 544–554, Feb. 2011.

[10] G. Covic and J. Boys, "Modern trends in inductive power transfer for transportation applications," *IEEE J. Emerg. Sel. Topics Power Electron.*, vol. 1, no. 1, pp. 28–41, Mar. 2013.

[11] C.-S. Wang, O. Stielau, and G. Covic, "Design considerations for a contactless electric vehicle battery charger," *IEEE Trans. Ind. Electron.*, vol. 52, no. 5, pp. 1308–1314, Oct. 2005.

[12] C.-Y. Huang, J. Boys, G. Covic, and M. Budhia, "Practical considerations for designing IPT system for EV battery charging," in *Proc. IEEE Veh. Power Propul. Conf.*, Sep. 2009, pp. 402–407.

[13] J. Huh, S. Lee, W. Lee, G. Cho, and C. Rim, "Narrow-width inductive power transfer system for online electrical vehicles," *IEEE Trans. Power Electron.*, vol. 26, no. 12, pp. 3666–3679, Dec. 2011.

[14] J. Huh, W. Lee, G.-H. Cho, B. Lee, and C.-T. Rim, "Characterization of novel inductive power transfer systems for on-line electric vehicles," in *Proc. IEEE 26th Annu. Appl. Power Electron. Conf. Expo.*, Mar. 2011, pp. 1975–1979.

[15] S. Lee, J. Huh, C. Park, N.-S. Choi, G.-H. Cho, and C.-T. Rim, "On-line electric vehicle using inductive power transfer system," in *Proc. IEEE Energy Convers. Congr. Expo.*, Sep. 2010, pp. 1598–1601.

[16] S. Choi, J. Huh, W. Lee, S. Lee, and C. Rim, "New cross-segmented power supply rails for roadway-powered electric vehicles," *IEEE Trans. Power Electron.*, vol. 28, no. 12, pp. 5832–5841, Dec. 2013.

[17] J. Sallan, J. Villa, A. Llombart, and J. Sanz, "Optimal design of ICPT systems applied to electric vehicle battery charge," *IEEE Trans. Ind. Electron.*, vol. 56, no. 6, pp. 2140–2149, Jun. 2009.

[18] M. Chigira, Y. Nagatsuka, Y. Kaneko, S. Abe, T. Yasuda, and A. Suzuki, "Small-size light-weight transformer with new core structure for contactless electric vehicle power transfer system," in *Proc. IEEE Energy Convers. Congr. Expo.*, Sep. 2011, pp. 260–266.

[19] O. C. Onar, J. M. Miller, S. L. Campbell, C. Coomer, C. White, and L. E. Seiber, "A novel wireless power transfer for in-motion EV/PHEV charging," in *Proc. IEEE 28th Annu. Appl. Power Electron. Conf. Expo.*, Mar. 2013, pp. 3073–3080.

[20] O. Onar, J. Miller, S. Campbell, C. Coomer, C. White, and L. Seiber, "Oak ridge national laboratory wireless power transfer development for sustainable campus initiative," in *Proc. IEEE Transp. Electr. Conf. Expo.*, Jun. 2013, pp. 1–8.

[21] J. Miller, O. Onar, C. White, S. Campbell, C. Coomer, L. Seiber, R. Sepe, and A. Steyerl, "Demonstrating dynamic wireless charging of an electric vehicle: The benefit of electrochemical capacitor smoothing," *IEEE Power Electron. Mag.*, vol. 1, no. 1, pp. 12–24, Mar. 2014.

[22] O. Onar, S. Campbell, P. Ning, J. Miller, and Z. Liang, "Fabrication and evaluation of a high performance sic inverter for wireless power transfer applications," in *Proc. IEEE Wide Bandgap Power Devices Appl. Workshop*, Oct. 2013, pp. 125–130.

[23] H. Wu, A. Gilchrist, K. Sealy, and D. Bronson, "A high efficiency 5 kW inductive charger for EVS using dual side control," *IEEE Trans. Ind. Informat.*, vol. 8, no. 3, pp. 585–595, Aug. 2012.

[24] K. Hall, M. Kesler, K. Kulikowski, and R. Fiorello. (2010, Nov. 4). Wireless energy transfer between a source and a vehicle. U.S. Patent 12/770 137. [Online]. Available: http://www.google.com/patents/US20100277121

[25] A. Bohori, A. Kumar, B. Worden, J. Bray, S. Ramachandrapanicker, A. Tiwari, and S. Bhat. (2011, Dec. 29). Power transfer system and method. U.S. Patent 12/822 232. [Online]. Available: https://www.google.com/patents/US20110315496

[26] A. Bohori, S. Ramachandrapanicker, C. Sihler, A. Tiwari, and S. Bhat. (2013, May 14). Contactless power transfer system. U.S. Patent 8 441 153. [Online]. Available: https://www.google.com/patents/US8441153

[27] A. Bohori, J. Bray, S. Ramachandrapanicker, and S. Bhat. (2013, Jul. 24). Contactless power transfer system and method. Eur. Patent EP20 110 159 292. [Online]. Available: https://www.google.com/patents/EP2369711A3?cl=en

[28] S. Lukic and Z. Pantic, "Cutting the cord: Static and dynamic inductive wireless charging of electric vehicles," *IEEE Electr. Mag.*, vol. 1, no. 1, pp. 57–64, Sep. 2013.

[29] "Wireless charging research activities around the world [society news]," *IEEE Power Electron. Mag.*, vol. 1, no. 2, pp. 30–38, Jun. 2014.

[30] N. Kar, K. Iyer, A. Labak, X. Lu, C. Lai, A. Balamurali, B. Esteban, and M. Sid-Ahmed, "Courting and sparking: Wooing consumers? Interest in the EV market," *IEEE Electr. Mag.*, vol. 1, no. 1, pp. 21–31, Sep. 2013.

[31] Sae taskforce j2954 on wireless charging and positioning standards looking to have final draft of guideline this year; significant industry involvement. (2012, Jan.). [Online]. Available: http://www.greencarcongress.com/2012/01/j2954-20120122.html

[32] J. Schneider. (2012, Jan.). Saej2954 overview and path forward. SAE. [Online]. Available: http://www.sae.org/smartgrid/sae-j2954-status_1-2012.pdf

[33] Sae international task force announces agreement on frequency of operation and power classes for wireless power transfer for its electric and plug-in electric vehicle guideline. SAE. (2013, Nov.). [Online]. Available: http://www.sae.org/servlets/pressRoom?OBJECT_TYPE=PressReleases&PAGE=sh owRelease&RELEASE_ID=2296

[34] M. Chinthavali, O. Onar, J. Miller, and L. Tang, "Single-phase active boost rectifier with power factor correction for wireless power transfer applications," in *Proc. IEEE Energy Convers. Congr. Expo.*, Sep. 2013, pp. 3258–3265.

[35] C.-S. Wang, G. Covic, and O. Stielau, "Investigating an LCL load resonant inverter for inductive power transfer applications," *IEEE Trans. Power Electron.*, vol. 19, no. 4, pp. 995–1002, Jul. 2004.

[36] J. T. Boys, C.-Y. Huang, and G. A. Covic, "Single-phase unity power-factor inductive power transfer system," in *Proc. IEEE Power Electron. Spec. Conf.*, Jun. 2008, pp. 3701–3706.
[37] H. Hao, G. Covic, M. Kissin, and J. Boys, "A parallel topology for inductive power transfer power supplies," in *Proc. IEEE 26th Annu. Appl. Power Electron. Conf. Expo.*, Mar. 2011, pp. 2027–2034.
[38] P. Ning, J. M. Miller, O. C. Onar, C. P. White, and L. D. Marlino, "A compact wireless charging system development," in *Proc. IEEE 28th Annu. Appl. Power Electron. Conf. Expo.*, Mar. 2013, pp. 3045–3050.
[39] J. Miller, C. White, O. Onar, and P. Ryan, "Grid side regulation of wireless power charging of plug-in electric vehicles," in *Proc. IEEE Energy Convers. Congr. Expo.*, Sep. 2012, pp. 261–268.
[40] R. Mecke and C. Rathge, "High frequency resonant inverter for contactless energy transmission over large air gap," in *Proc. IEEE 35th Annu. Power Electron. Spec. Conf.*, Jun. 2004, vol. 3, pp. 1737–1743.
[41] J. Miller, O. Onar, and M. Chinthavali, "Primary-side power flow control of wireless power transfer for electric vehicle charging," *IEEE J. Emerg. Sel. Topics Power Electron.*, vol. 3, no. 1, pp. 147–162, Mar. 2015.
[42] R. Bosshard, J. Kolar, J. Muhlethaler, I. Stevanovic, B. Wunsch, and F. Canales, "Modeling and η-α-Pareto optimization of inductive power transfer coils for electric vehicles," *IEEE J. Emerg. Sel. Topics in Power Electron.*, vol. 3, no. 1, pp. 50–64, Mar. 2015.
[43] H. Hao, G. Covic, and J. Boys, "An approximate dynamic model of LCL-T-based inductive power transfer power supplies," *IEEE Trans. Power Electron.*, vol. 29, no. 10, pp. 5554–5567, Oct. 2014.
[44] C.-Y. Huang, J. James, and G. Covic, "Design considerations for variable coupling lumped coil systems," *IEEE Trans. Power Electron.*, vol. 30, no. 2, pp. 680–689, Feb. 2015.
[45] H. Wu, A. Gilchrist, K. Sealy, P. Israelsen, and J. Muhs, "Design of symmetric voltage cancellation control for LCL converters in inductive power transfer systems," in *Proc. IEEE Int. Electr. Mach. Drives Conf.,* May 2011, pp. 866–871.
[46] C.-S. Wang, G. Covic, and O. Stielau, "Power transfer capability and bifurcation phenomena of loosely coupled inductive power transfer systems," *IEEE Trans. Ind. Electron.*, vol. 51, no. 1, pp. 148–157, Feb. 2004.
[47] J. T. Boys, G. A. Covic, and A. W. Green, "Stability and control of inductively coupled power transfer systems," *Electr. Power Appl., IEE Proc.*, vol. 147, no. 1, pp. 37–43, Jan. 2000.
[48] Z. Pantic, S. Bai, and S. Lukic, "ZCS LCC—Compensated resonant inverter for inductive-power-transfer application," *IEEE Trans. Ind. Electron.*, vol. 58, no. 8, pp. 3500–3510, Aug. 2011.
[49] G. Covic, J. T. Boys, A. M. W. Tam, and J. C. H. Peng, "Self tuning pick-ups for inductive power transfer," in *Proc. IEEE Power Electron. Spec. Conf.*, June 2008, pp. 3489–3494.
[50] N. Keeling, G. Covic, and J. Boys, "A unity-power-factor IPT pickup for high-power applications," *IEEE Trans. Ind. Electron.*, vol. 57, no. 2, pp. 744–751, Feb. 2010.
[51] G. Elliott, S. Raabe, G. Covic, and J. Boys, "Multiphase pickups for large lateral tolerance contactless power-transfer systems," *IEEE Trans. Ind. Electron.*, vol. 57, no. 5, pp. 1590–1598, May 2010.
[52] M. Budhia, G. Covic, and J. Boys, "Design and optimization of circular magnetic structures for lumped inductive power transfer systems," *IEEE Trans. Power Electron.*, vol. 26, no. 11, pp. 3096–3108, Nov. 2011.
[53] R. Steigerwald, "A comparison of half-bridge resonant converter topologies," *IEEE Trans. Power Electron.*, vol. 3, no. 2, pp. 174–182, Apr. 1988.
[54] H. Ma and W. Zhou, "Modeling a current source push-pull resonant converter for loosely coupled power transfer systems," in *Proc. IEEE 30th Annu. Conf. Ind. Electron. Soc.*, Nov. 2004, vol. 2, pp. 1024–1029.
[55] C.-S. Wang, O. Stielau, and G. Covic, "Load models and their application in the design of loosely coupled inductive power transfer systems," in *Proc. Power Syst. Technol., Int. Conf.*, 2000, vol. 2, pp. 1053–1058.
[56] C.-S. Wang, G. Covic, and O. Stielau, "General stability criterions for zero phase angle controlled loosely coupled inductive power transfer systems," in *Proc. IEEE 27th Annu. Conf. Ind. Electron. Soc.*, 2001, vol. 2, pp. 1049–1054.
[57] M. Budhia, J. Boys, G. Covic, and C.-Y. Huang, "Development of a single-sided flux magnetic coupler for electric vehicle IPT charging systems," *IEEE Trans. Ind. Electron.*, vol. 60, no. 1, pp. 318–328, Jan. 2013.
[58] A. Zaheer, D. Kacprzak, and G. Covic, "A bipolar receiver pad in a lumped IPT system for electric vehicle charging applications," in *Proc. IEEE Energy Convers. Congr. Expo.*, Sep. 2012, pp. 283–290.
[59] M. Kissin, J. Boys, and G. Covic, "Interphase mutual inductance in polyphase inductive power transfer systems," *IEEE Trans. Ind. Electron.*, vol. 56, no. 7, pp. 2393–2400, Jul. 2009.
[60] M. Budhia, G. Covic, and J. Boys, "Design and optimization of circular magnetic structures for lumped inductive power transfer systems," *IEEE Trans. Power Electron.*, vol. 26, no. 11, pp. 3096–3108, Nov. 2011.
[61] M. Budhia, G. Covic, and J. Boys, "A new IPT magnetic coupler for electric vehicle charging systems," in *Proc. IEEE 36th Annu. Conf. Ind. Electron. Soc.*, Nov. 2010, pp. 2487–2492.
[62] H. Wheeler, "Simple inductance formulas for radio coils," *Radio Eng., Proc. Inst.*, vol. 16, no. 10, pp. 1398–1400, Oct. 1928.
[63] C. Park, S. Lee, G. Cho, and C. Rim, "Innovative 5-m-off-distance inductive power transfer systems with optimally shaped dipole coils," *IEEE Trans. Power Electron.*, vol. 30, no. 2, pp. 817–827, Feb. 2015.
[64] C. Tang, X. Dai, Z. Wang, Y. Sun, and A. Hu, "Frequency bifurcation phenomenon study of a soft switched push-pull contactless power transfer system," in *Proc. IEEE 6th Ind. Electron. Appl. Conf.*, Jun. 2011, pp. 1981–1986.
[65] C.-Y. Huang, *A Low Cost ICPT Power Supply*. Auckland, New Zealand: Electrical and Computer Engineering, Univ. of Auckland, 2006
[66] M. Borage, S. Tiwari, and S. Kotaiah, "Analysis and design of an LCL-T resonant converter as a constant-current power supply," *IEEE Trans. Ind. Electron.*, vol. 52, no. 6, pp. 1547–1554, Dec. 2005.
[67] F. Musavi, M. Edington, W. Eberle, and W. Dunford, "Energy efficiency in plug-in hybrid electric vehicle chargers: Evaluation and comparison of front end ac-dc topologies," in *Proc. IEEE Energy Convers. Congr. Expo.*, Sep. 2011, pp. 273–280.

Bryan Esteban (M'15) received the B.A.Sc. and M.A.Sc. degrees in electrical and computer engineering from the University of Windsor, Windsor, ON, Canada, in 2011 and 2014, respectively.

His research interests include high power and efficiency power electronics, resonant power conversion, and inductive power transfer. The work described in this paper is a first of its kind in Canada and was completed by him with the support of his co-authors over a period spanning January 2013 to August 2014. During this time, he worked as a Lead Researcher of wireless EV charging systems at the Center for Hybrid Automotive Research and Green Energy.

Maher Sid-Ahmed received the B.A.Sc. degree from the University of Alexandria, Alexandria, Egypt, in 1968, and the M.A.Sc. and Ph.D. degrees from the University of Windsor, Windsor, ON, Canada, in 1971 and 1973, respectively.

He is the Author of a book entitled "*Image Processing, Theory, Algorithms and Architectures*" (New York, NY, USA: McGraw-Hill, 1995). He holds four U.S. patents and has published 80 journal papers. Supervised and graduated more than 60 M.A.Sc. and Ph.D. students. His research interest includes image processing, machine vision, meteorology using stereo vision, systolic structures, hardware realization for real-time processing, OCR including hand writing recognition, and now wireless electricity.

Narayan C. Kar (S'97–M'00–SM'07) received the B.Sc. degree in electrical engineering from the Bangladesh University of Engineering and Technology, Dhaka, Bangladesh, in 1992, and the M.Sc. and Ph.D. degrees in electrical engineering from the Kitami Institute of Technology, Hokkaido, Japan, in 1997 and 2000, respectively.

He is currently an Associate Professor at the Electrical and Computer Engineering Department, University of Windsor, Windsor, ON, Canada, where he holds the Canada Research Chair position at the Electrified Transportation Systems. His research interests include the analysis, design, and control of electrical machines for electric and hybrid electric vehicles, charging systems, testing, and performance analysis of batteries and development of optimization techniques for hybrid energy management system.